Mongold, E., and Baker, J. W. (2024). "Probabilistic Regional Liquefaction Hazard and Risk Analysis: A Case Study of Residential Buildings in Alameda, California." Natural Hazards Review, 25(4), 04024039. *https://doi.org/10.1061/NHREFO.NHENG-2078*

PROBABILISTIC REGIONAL LIQUEFACTION HAZARD AND RISK ANALYSIS: A CASE STUDY OF RESIDENTIAL BUILDINGS IN ALAMEDA, CA

Emily Mongold[1] and Jack W. Baker, Ph.D.[2]

[1]Ph.D. Researcher. Dept. of Civil Engineering and Environmental Engineering, Stanford Univ., 439 Panama Mall, Stanford, CA 94305. Email: emongold@stanford.edu
[2]Professor. Dept. of Civil Engineering and Environmental Engineering, Stanford Univ., 439 Panama Mall, Stanford, CA 94305

ABSTRACT

The impact of liquefaction on a regional scale is not well understood or modeled with traditional approaches. This paper presents a method to quantitatively assess liquefaction hazard and risk on a regional scale, accounting for uncertainties in soil properties, groundwater conditions, ground shaking parameters, and empirical liquefaction potential index (LPI) equations. The regional analysis is applied to a case study to calculate regional occurrence rates for the extent and severity of liquefaction and to quantify losses resulting from ground shaking and liquefaction damage to residential buildings. We present a regional-scale metric to quantify the extent and severity of liquefaction. A sensitivity analysis on epistemic uncertainty indicates that the two most important factors on output liquefaction maps are the empirical liquefaction equation, emphasizing the necessity of incorporating multiple equations in future regional studies, and the ground motion model, highlighting the same necessity for the peak ground acceleration input. Furthermore, the disaggregation of seismic sources reveals that triggering earthquakes for various extents of liquefaction originate from multiple sources, though primarily nearby faults and large magnitude ruptures. This finding indicates the value of adopting regional probabilistic analysis in future studies to capture the diverse sources and spatial distribution of liquefaction.

INTRODUCTION

Liquefaction, a type of ground failure during earthquakes, can cause major damage, but our ability to model the phenomenon on a regional scale is limited. Much of liquefaction research focuses on triggering at individual locations, with predictive equations fit to empirical data (e.g. Iwasaki et al. 1978; Robertson and Campanella 1985; Moss et al. 2006). Many empirical liquefaction equations output the liquefaction potential index (LPI). This metric indicates the likelihood or severity of liquefaction, generally interpreted through thresholds (Iwasaki et al. 1978) or conversion to probability (e.g. Li et al. 2006). LPI is calculated at a single borehole location; however, impacts of liquefaction are seen on a regional level. In order to predict losses and impacts, a unified workflow is necessary to model hazard, damage, and loss.

Research within geotechnical engineering mostly investigates triggering (e.g. Holzer et al. 2011; Todorovic and Silva 2022; Zhu et al. 2017) or empirical analysis of past liquefaction impacts (e.g. Cubrinovski et al. 2011; Cubrinovski et al. 2012; Cubrinovski et al. 2017). For single locations, Goda et al. (2011) presents a probabilistic liquefaction hazard analysis method that outputs the annual rate of exceedance for a given LPI, accounting for the probability of each earthquake rupture that may trigger liquefaction. Some work has been done to expand the methods to further assess the severity of liquefaction, probability of liquefaction, impacts on structures, and regional analysis (National Academies of Sciences, Engineering, and Medicine 2021). For damage to structures, Setiawan et al. (2017) have considered the damage as the angle of tilt, though it is not predictive or translated into monetary loss. Vulnerability curves have been fit to damage data of buildings based on LPI (Geyin et al. 2020).

Some studies have translated to a regional scale through combinations of multiple data sources (e.g. Holzer et al. 2002; Toprak and Holzer 2003; van Ballegooy et al. 2015), and various liquefaction metrics have been used in concert to determine damages (e.g. Koutsourelakis et al. 2002; Bird et al. 2006; Sahir and Pak 2010; Holzer et al. 2011). Many studies have been compared in their ability to predict liquefaction manifestation at individual sites (Bullock et al. 2023), while other studies look at regional probabilities of liquefaction (e.g. Geyin and Maurer 2020; Maurer et al. 2014). Many regional liquefaction studies use geologic units to determine underlying soil susceptibility (e.g. Yilmaz et al. 2021; Greenfield and Grant 2022) or interpolate soil properties only within geologic units (e.g. Baise et al. 2006; Wang and Chen 2018). This is useful as soil units are known at large scales, represent similar soil types, and can inform studies that point to locations worth investigating more closely. Others argue for spatial interpolation approaches, finding that geologic units are not very distinct (Lenz and Baise 2007). A few studies have generated simulated soil properties across a region using random field methods (e.g. Phoon and Kulhawy 1999; Baker and Faber 2008; Wang et al. 2017).

Liquefaction hazard, damage, and loss have mostly been studied separately, making it difficult to run a complete regional analysis on available data. Though many liquefaction metrics exist, their use is limited by data availability. Each metric is based on different input data, from geologic information, triggering earthquake information, or site analysis. Many models have been proposed to perform regional studies without detailed geotechnical data (e.g. Zhu et al. 2015; Zhu et al. 2017; Bozzoni et al. 2021; Todorovic and Silva 2022) that are useful in loss estimation. For the proposed methodology, we employ building-level fragility functions for LPI, which rely on more detailed geotechnical methods. However, other metrics could be used in a similar methodology so long as the metric has corresponding building-level fragility relationships. For soil map generation, uncertainty is often not included, and refined spatial scales without improved data may introduce additional uncertainty (Wang et al. 2017). Regional assessment of liquefaction has been addressed in past studies (e.g. Geyin and Maurer 2020; Maurer et al. 2014), including some that consider the importance of groundwater depth (e.g. Chung and Rogers 2013; Grant et al. 2021), though none have been fully probabilistic considering the impact of the earthquake rupture and other uncertain inputs on the outputs. No studies perform a comprehensive probabilistic liquefaction hazard and risk analysis (National Academies of Sciences, Engineering, and Medicine 2021). Some studies have performed probabilistic risk analyses on single locations (e.g. Kramer and Mayfield 2007; Makdisi 2021). These studies motivate the inclusion of multiple earthquake intensities in risk analysis, though they are not extended to calculate losses, and are not regional in scope.

In this work, we utilize limited measured data to determine liquefaction potential on a regional scale and perform a loss analysis from liquefaction and ground shaking, creating a unified process that accounts for uncertainty in modeling parameters. This methodology is focused on the ability to run full risk analysis, meaning that the work includes hazard and loss simulations. For loss analysis, building data are necessary, as well as a fragility function, or mathematical connection between a hazard metric and damage or loss. In this case, we utilize a fragility function that relates LPI to residential building loss (Geyin et al. 2020), which requires the simulation of LPI across the study area. We use the term ‘regional’ to specify that the analysis is performed across a study area, not at a single location, similar to the convention in Kim et al. 2021. A regional-scale metric is presented to quantify the extent and severity of liquefaction hazard. This metric provides the ability to disaggregate the source of risk. This paper aims to understand the range of regional liquefaction potential given uncertainty in modeling choices, or epistemic uncertainty, and to unify the process to consider regional liquefaction occurrence and losses. We do this by utilizing cone penetration test (CPT)-based LPI calculations and including uncertainty in model inputs on a regional scale. The impact of epistemic uncertainty on the analysis output is quantified through a distance-based general sensitivity analysis. Finally, disaggregation of the liquefaction hazard highlights the earthquake sources contributing to widespread liquefaction. This approach is demonstrated using a case study on the island of Alameda in the San Francisco Bay in California.

METHODS

The goal of this analysis is to probabilistically characterize regional liquefaction hazard and risk. We do this by varying input properties such as the ground motion model, the depth to groundwater, and the variance in soil properties, through a series of Monte Carlo simulations. A 2D grid is placed across the study area, input values are simulated, and output values are obtained at each grid point. The array of output values is used to quantify epistemic, or modeling, uncertainty from each of the varied input parameters. Liquefaction risk is simulated based on expected loss over the probabilistic rupture scenarios.

Fig. 1 illustrates the calculation process for one simulation, with inputs for ground motions, groundwater, and soil properties. Shown under ‘Soil properties’ we use cone penetration test data to simulate possible 3D soil profiles of the soil grid over the case study area. Shown under ‘Ground motions,’ we use a seismic hazard model to create ground-shaking simulations of peak ground acceleration (PGA) across the case study area. Under ‘Groundwater level’ we interpolate from known datapoints and add variation to that surface to create simulations of the groundwater surface. In the fourth column, ‘Liquefaction potential,’ the results from the three previous columns are inputs for evaluating the liquefaction potential index (LPI) equation at each gridpoint across the study area to produce an output map of LPI. This regional work is distinct from point- or location-based calculations as it is performed at simulated data locations and not just where CPT data is available. In the last column, ‘Hazard and risk analysis,’ we convert the LPI at each residential building to an expected loss ratio. Since parameters are varied to produce each input, multiple maps of liquefaction potential and damage are produced as this workflow is repeated.

This methodology requires input data regarding the faults in the area, groundwater data, liquefaction-relevant soil data such as CPT tests, and exposure data of buildings or assets that may incur damage. While individual simulation methods may be replaced within the framework, these are the minimum necessary inputs to run the simulations. The three categories of input to the liquefaction potential calculation are soil properties, ground motions, and groundwater level. These are expanded upon in the following sections, followed by the methods for the LPI calculations, regional hazard and risk analysis, and sensitivity analysis on the outputs.

Soil Properties

The soil properties simulated for this workflow are cone penetration test (CPT) borehole measurements of tip resistance, q_c, and sleeve friction, f_s, to a depth of 20m. Measured CPT data are

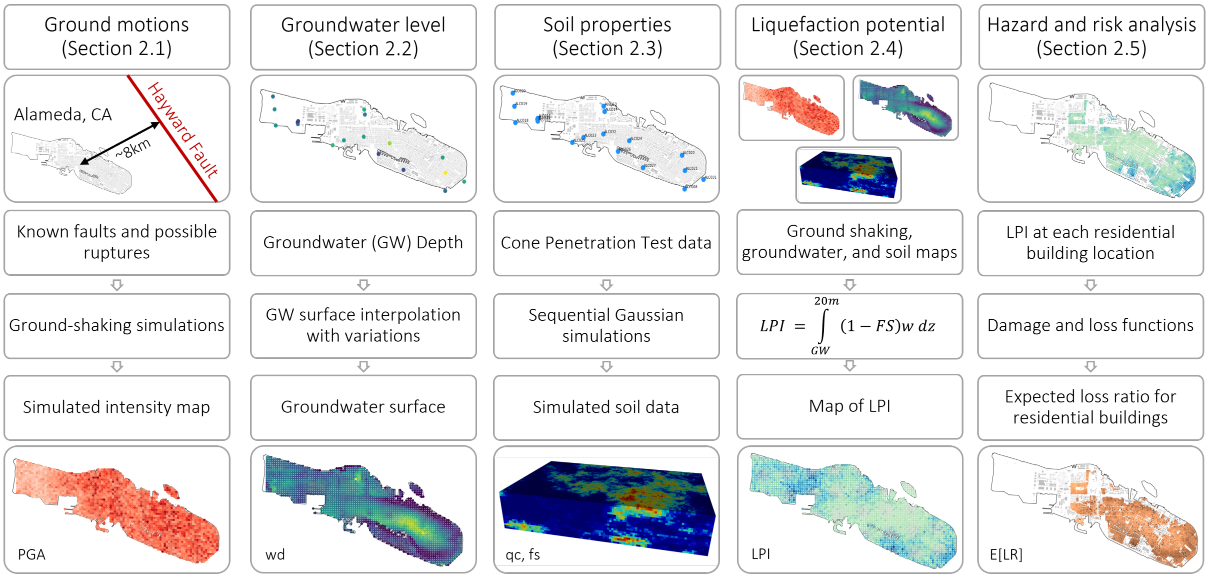

Fig. 1. Graphical representation of the process for each Monte Carlo simulation. From left to right, the columns show the generation of ground motions from possible ruptures, the groundwater surface interpolated from measured groundwater depths, the soil properties simulated on a 3D grid to create interpolated CPT data, the combination of the three inputs to generate a 2D map of liquefaction potential, and the application of liquefaction onto buildings to output expected losses.

obtained at multiple sites across the study area. The q_c and f_s values at unmeasured locations are simulated via spatially correlated sampling. This process results in output 3D maps of q_c and f_s values that cover the case study area to a depth of 20m.

A random field method is implemented to generate 3D soil maps (Wang et al. 2017). To maintain directionality, a model input (termed a variogram) specifies the decay of variable correlation with distance in each direction. The variogram parameters designate the correlations in the horizontal and vertical directions, as well as the portion of unexplained stochasticity, referred to as the variogram nugget (Fenwick et al. 2014). These parameters may be estimated from the measured data or from published recommendations (e.g. Phoon and Kulhawy 1999). The uncertainty in each of these parameter assignments determines the range applied. Simulation may be performed many ways, but it is important that the directional anisotropy of the input parameters is sustained to simulate soil layering (e.g. Wang et al. 2017).

Based on previous research in the region, detail about the soil is lost when separating geologic deposits, so interpolating across geologic deposits is a good representation of the soil, especially when only few boreholes exist in a separate geologic deposit (Lenz and Baise 2007). In addition, the difference in vertical and horizontal correlations in the soil variogram create layering in the soil based on the correlation present in the borehole data. Generally, our maps of high liquefaction hazard and high liquefaction damages correspond to the geologic deposits and susceptibility maps from previous studies (Knudsen et al. 2000; Holzer et al. 2006; Lenz and Baise 2007).

The soil property of time-averaged shear wave velocity values over the first 30m of soil, $V_{s,30}$, is necessary for ground motion simulations. To ensure consistency with simulated soil models, the $V_{s,30}$ is best determined through direct measurement in CPT data. In cases where the shear wave velocity is not measured, approximation from CPT data can be performed (e.g. Andrus et al. 2007). In either case, the values can be interpolated and extrapolated to points in and around the site that will be used for ground motion simulation.

Ground Motions

The first modeling step is performing earthquake simulations. Earthquake ruptures are simulated from a seismic source model that accounts for nearby known faults and earthquake sources. The number of sampled ruptures will determine the minimum total number of simulations performed for the probabilistic liquefaction analysis. Recommended minimum earthquake magnitudes to consider for probabilistic liquefaction hazard analysis are M4.5 for impact to distributed infrastructure and M5.0 for buildings (Green and Bommer 2019).

To generate an intensity measure field across the study area, a ground motion model (GMM) is applied to each generated rupture (e.g. Abrahamson et al. 2014; Boulanger and Idriss 2014; Chiou and Youngs 2014). Multiple empirical models should be selected and weighted to represent an epistemic uncertainty distribution. These weights are the assigned probabilities of selecting each model during Monte Carlo sampling. The GMM predicts the mean log intensity measure ($\mu_{\ln IM}$), where IM is peak ground acceleration (PGA) in this study. Stochasticity appears in the IM values by virtue of the probabilistic seismic hazard analysis, which uses spatially correlated between- and within-event residuals, ΔB_j and $\Delta W_{i,j}$, respectively, to obtain IM values across the region of interest, as

$$\ln IM_{i,j} = \mu_{\ln IM}(site_i, rup_j) + \Delta B_j + \Delta W_{i,j} \tag{1}$$

where μ signifies the mean value and is a function of site variables, $site_i$, and rupture variables, rup_j. The required inputs vary depending on the chosen ground motion model, but always include the rupture magnitude and distance to each location. The site variable also includes time-averaged shear wave velocity values over the first 30m of soil, $V_{s,30}$, across the study area. Ground motions are interpolated from a sparse grid for computational efficiency and due to low spatial variation within the study area. Since $V_{s,30}$ is a depth-averaged metric, it is not as locally varying as the other soil properties. Thus, we utilize one interpolation across the region for all simulations. Through the ground motion simulations, the IM value varies across the study area and with every simulation. The magnitude of the rupture, M_j, the average site-to-source distance, $R_{i,j}$, and annual rates of return, $\lambda_{rup,j}$ are also retained for later disaggregation and risk calculations.

Groundwater Level

The groundwater is important to the analysis because the soil must be below the groundwater table to liquefy. Groundwater data must be obtained or interpolated for the entire study area. Measurements are taken as true values for interpolation. In order to interpolate from a few measurements of groundwater, the depth of groundwater at points across the study area and the elevation across the study area are necessary. Tidal fluctuations, seasonal changes, and other temporal variation in groundwater levels are not typically recorded, so uncertainty may be added globally, later in the process. If multiple sets of measurements are taken in time, the variation can be used to constrain fluctuation or only the newest measurements can be considered as present-day water level, depending on whether measurement variation is attributed to tide, season, and other environmental factors, or to a changing mean value over time.

Geospatial interpolation is used to determine the groundwater level at gridpoints across the study

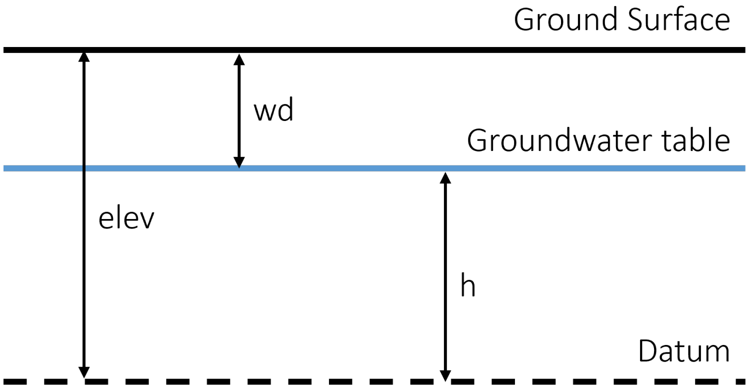

Fig. 2. Graphic representation of the groundwater measurements necessary for interpolation.

area (e.g. Greenfield and Grant 2022; Beyzaei et al. 2020). The interpolation scheme is chosen based on the soil conditions in the area of study, and whether the groundwater is flux-controlled, depending on free water level, or head-controlled, being affected by changes in elevation. Only one of the interpolation schemes should be used if this can be constrained by local studies of the geologic conditions, considering data on recharge, hydraulic conductivity, aquifer thickness, and distance between hydrological boundaries (Mussa et al. 2020). If groundwater is head-controlled, then measurements of depth-to-groundwater, wd, can be interpolated across the study area. In cases where the groundwater is flux-controlled, the elevation is necessary to interpolate from a datum. As illustrated in Fig. 2, h, or the height of groundwater from a datum, can be calculated as $h = elev - wd$ at each point, where $elev$ is the ground elevation relative to the datum. This height variable, h, is then used as the metric for interpolation, and depth to groundwater is back-calculated as $wd = elev - h$. The addition of variation may be employed with a global (uniform) shift of the generated groundwater table. This variation represents uncertainty in the tides, seasons, and changes over time of water level.

Liquefaction Potential

The liquefaction potential simulation uses simulated ground motions, groundwater levels, and soil properties to output LPI values at each gridpoint. Empirical LPI models must be chosen, just as the ground motion models are chosen to simulate ground motions. Probabilities are assigned to each model, and used to sample a model for each simulation. The LPI calculation is performed at each gridpoint within the study area as

$$LPI = \int_{wd}^{20m} (1 - FS) \cdot w(z) dz \tag{2}$$

where wd is the depth to groundwater, FS is the factor of safety against liquefaction, and $w(z)$ is the weighting factor as a function of depth from the surface, z (Iwasaki et al. 1978). To account for the need for saturation for liquefaction triggering, the integration is performed from the depth to groundwater down to the 20m maximum depth. Liquefaction calculation methods often utilize the simplified procedure, where the factor of safety against liquefaction, FS is

$$FS = CRR/CSR \tag{3}$$

or, the ratio of cyclic resistance ratio (CRR) of the soil to the cyclic stress ratio (CSR) from ground shaking. Both CRR and CSR are obtained from the empirical models, accounting for the input q_c, f_s, M and wd values. When $FS < 1$, there is liquefaction triggering in that element of soil (National Academies of Sciences, Engineering, and Medicine 2021). The linear weighting function, $w(z)$ is defined as

$$w(z) = 10 - 0.5z \tag{4}$$

where z is the depth measured down from the ground surface. This procedure is repeated for each gridpoint and each Monte Carlo simulation.

Hazard and Risk Analyses

The generated LPI maps for the study area, given varied input parameters, can be used to probe the extent and severity of liquefaction, and the impacts on residential buildings and resulting losses. This section discusses four main regional analyses performed in this study: rates of liquefaction, regional severity metrics, disaggregation of regional risk, and expected loss due to liquefaction.

The first step in this hazard analysis is calculating the rate of liquefaction through the rates of their triggering ruptures. Each earthquake rupture has an associated annual rate of occurrence, $\lambda_{rup,j}$, as described above in the Ground Motions section. LPI is converted to a probability of liquefaction through an empirical equation by Li et al. (2006). This probability can then be applied such that for each simulated earthquake rupture, rup_j, each point on the site area grid has a probability of liquefaction, conditional on the rupture, $P(L|rup_j)$. Thus, the annual rate of liquefaction, λ_L, at a point is defined by

$$\lambda_L = \sum_{j=1}^{n_{rup}} P(L|rup_j) \cdot \lambda_{rup,j} \tag{5}$$

where n_{rup} is the total number of ruptures. In this case, liquefaction, L, is treated as a binary event without variance in severity.

In some contexts it is useful to maintain the LPI as a proxy for severity, instead of condensing liquefaction to this binary output. To this end, the LPI outputs can be used to calculate a regional severity metric. This work expands the probabilistic framework of Goda et al. (2011) for liquefaction triggering at a single site to a regional metric. Instead of a threshold alone, a portion of land area is used in concert with LPI threshold to proxy extent and severity of liquefaction, calculated for a given rupture j as

$$A_{LPI\geq lpi,j} = \frac{\sum_{i=1}^{n_{gdpt}} [LPI_{i,j} > lpi]}{n_{gdpt}} \tag{6}$$

where $[\cdot]$ is the indicator function, equal to 1 if true and 0 if false, n_{gdpt} is the number of gridpoints within the case study area, $LPI_{i,j}$ is the LPI at gridpoint i from rupture j, and $A_{LPI\geq lpi}$ is the fractional area exceeding a chosen LPI threshold, lpi. The rate for fractions of land area exceeding various LPI thresholds, our proposed regional-scale metric, can then be calculated as

$$\lambda_{A_{LPI\geq lpi}>a} = \sum_{j=1}^{n_{rup}} [A_{LPI\geq lpi,j} > a] \cdot \lambda_{rup,j} \tag{7}$$

where a is the area fraction threshold of interest. The summation is performed over all ruptures considered in the analysis. This rate is a useful regional metric to communicate the probability of an extent and severity of liquefaction of interest. This regional metric gives us the ability to find equivalent hazard rates of different severities and extents, which is useful to find equivalent rate impacts or to choose hazard levels to consider for a region. This calculation can also inform whether higher rate events are generally getting more extensive or more severe, and what the limits may be for extent and severity.

One use of this regional metric is to identify ruptures likely to cause outcomes of interest. Within seismic hazard analysis, it is common to disaggregate the contribution of various earthquake sources to the earthquake hazard for a given intensity measure at a single site (Baker et al. 2021). Here we apply the concept to disaggregate the contribution of triggering earthquakes to the regional liquefaction hazard. Disaggregation is performed on magnitudes and distances of earthquakes that exceed various areas of LPI thresholds. Disaggregation on rupture magnitude and distance is calculated as

$$P(M = m, R = r | A_{LPI \geq lpi} \geq a) = \frac{\lambda_{A_{LPI \geq lpi} \geq a, M=m, R=r}}{\lambda_{A_{LPI \geq lpi} \geq a}} \tag{8}$$

where $\lambda_{A_{LPI \geq lpi} \geq a}$ is the rate of area exceeding given LPI and area thresholds, lpi and a respectively, and $\lambda_{A_{LPI \geq lpi} \geq a, M=m, R=r}$ is the rate of that area being exceeded with the source being of a given magnitude, M and source-site distance, R. Distances are computed as the mean source-to-site distance for all points in the study area, to give an indication of average distance. This is equivalent to using the distance to the centroid of the study area. In practice, the sources are grouped into ranges of magnitudes and distances, such as M7.0 to M7.5 at a distance of 10 to 20 km. Through the rupture information retained from the ground motion simulation, the sources that contribute to larger extent and severity combinations are determined as those with the highest probability as calculated in Eq. 8. This calculation determines what ruptures contribute the most to the outcome of interest.

We next perform a risk analysis to quantify damages to buildings from ground shaking and liquefaction. Risk analysis often involves determining the damage state, $DS_{j,k}$, of each building, k, for rupture j and translating that $DS_{j,k}$ to a loss ratio, $LR_{j,k}$. This translation is often performed using a fragility function to define the probability of being in a categorical damage state as a function of the intensity measure, $P(DS_k \geq ds | IM_k = im)$. A fragility function is employed for damage from ground shaking, with the IM being PGA. In the case of Hazus fragility functions, they depend on building code level and structural type (FEMA 2020). Alternatively, a single-step model may be used, which directly computes loss ratio as a function of intensity measure, $LR_k = f(IM_k)$. A single-step model is employed for loss from liquefaction, approximated from the vulnerability function used in Geyin et al. 2020. In either case, the requisite models will be a function of building type, which may depend on factors such as structural system and year of construction. The liquefaction vulnerability function applies to all residential buildings due to aggregation of data. If the liquefaction function includes all damages (i.e. from ground shaking and liquefaction), then the total loss ratio should be the maximum of the two.

The loss ratio functions are applied to the buildings based on the LPI and PGA of the nearest grid point, and weighted based on the annual rate of the triggering earthquake rupture, λ_{rup}. With this weighting, the expected annual loss ratio is calculated as

$$E[LR_k] = \sum_{j=1}^{n_{rup}} LR_{j,k} \cdot \lambda_{rup,j} \tag{9}$$

where n_{rup} is the number of ruptures included in the analysis, and $\lambda_{rup,j}$ is the occurrence rate of earthquake rupture j. The expected annual loss ratio from liquefaction, $E[LR_{liq,k}]$ is similarly calculated as

$$E[LR_{liq,k}] = \sum_{j=1}^{n_{rup}} LR_{liq,j,k} \cdot \lambda_{rup,j} \tag{10}$$

with the loss ratio from liquefaction for each rupture, j, and building, k represented by $LR_{liq,j,k}$ and the rate of the earthquake rupture as $\lambda_{rup,j}$. For each rupture, j, the total regional loss can be calculated as

$$Loss_j = \sum_{k=1}^{n_{bld}} LR_{j,k} \cdot BV_k \tag{11}$$

where LR_k is the loss ratio of building k and BV_k is the total building value of building k. The sum is aggregated over the total number of buildings, n_{bld}, to obtain regional loss over the case study area for rupture j.

Sensitivity Analysis

With the outputs of the Monte Carlo simulations, a sensitivity analysis is performed to determine the most important parameters to explain the variation in LPI. Distance-based general sensitivity analysis (DGSA) defines the sensitivity as the distance between cumulative distribution functions of input variables for clusters with similar output values (Fenwick et al. 2014). The number of clusters is determined by the user. High sensitivity values signify that the output clusters have notably different distributions of a given input, indicating that the input is influential. The number of clusters is chosen such that cluster groups have enough simulations to reflect a common output pattern. The sensitivity analysis only includes modeling parameters, or epistemic uncertainty, which affect the model outcome. Aleatory uncertainty remains, and liquefaction severity is affected by the triggering event, as demonstrated by the disaggregation calculations. This sensitivity analysis informs where we could use additional parameter constraints in modeling and what parameters should be considered in future studies, as they affect the liquefaction potential predictions.

DGSA is chosen for the sensitivity analysis due to its applicability to spatial data with high dimensions and non-linear relationships. The method is also flexible to accept existing simulations without prescribing sets of inputs, which would require significant additional computation. DGSA works by grouping outputs into clusters. The number of clusters should be chosen such that they capture output variability. In our case, three clusters were sufficient to capture different levels of liquefaction across the case study area, and additional clusters captured few simulations and were not found to be distinct or interpretable. The three clusters were generally found to indicate low, medium, and high overall liquefaction extent across the study area. The sensitivity value for each input is the normalized area between the cumulative distribution functions (CDFs) of the input parameter between the clusters. If the CDF for each cluster is similar, then that input parameter has a low sensitivity value and is not a good predictor of the output cluster. However, if the area between CDFs is large, then that parameter has a higher value and is a good predictor of the output cluster, which in our case represents extent of liquefaction. For stability, we first perform principal component analysis on the outputs and consider the principal components that explain 99% of the variance for analysis. Using boostrapping, 90% confidence intervals can be determined for the sensitvity parameter.

CASE STUDY APPLICATION

The above process is applied to a case study in Alameda, California: a liquefaction-susceptible city on an island in the San Francisco Bay (Witter et al. 2006). The USGS has public cone penetration test data for this area (U.S. Geological Survey 2002). Alameda is surrounded by faults, with the San Andreas to the southwest and the Hayward to the northeast, making it susceptible to earthquake impacts. Losses to residential buildings are considered here, though losses may also occur in other systems such as commercial buildings and infrastructure systems.

The study area is divided into gridpoints with a spacing of 0.1km, for a total of 2063 gridpoints. For each of 2423 earthquake rupture simulations described below, a simulation of the soil model, the groundwater surface, and liquefaction manifestation are sampled and used to generate a simulation of LPI at each grid point. These results are then used to compute the rate of liquefaction, regional severity, disaggregation, and loss analysis. The implementation of the proposed analysis is described in further detail in the following subsections.

Soil Properties

CPT data are available from 21 boreholes in the same dataset as the groundwater measurements (U.S. Geological Survey 2002). While the measurements are taken every 5cm of depth, they are averaged into 1m sections for computational efficiency and because this did not significantly change the outputs. A similar study aggregated at 0.2m (Wang et al. 2017). Sequential Gaussian simulations are utilized to generate the 3D soil maps at non-measured locations. These soil maps are on a grid of 0.1km x 0.1km x 1m, with the highest resolution in the vertical direction to capture layering in the soil. The two soil parameters, q_c and f_s, are assumed to be independent, but simulated with the same variogram parameters.

The soil properties variogram ranges dictate how far in the horizontal and vertical directions known values impact unknown values. The variogram nugget indicates the portion of unexplained stochasticity. The variogram ranges for the grid vary from 1.5 - 3.0km in the horizontal direction and 10 - 20m in the vertical direction, and the nugget varies from 0.0001 - 0.2. The higher variation vertically reflects the faster variation in soil properties with depth, due to layering during deposition. The estimation of the variogram is performed on the measured data and has uncertainty depending on tolerance levels and lag data included. Multiple parameter estimates fit the data well, and estimates are geared to the closest distance points. To test the sensitivity of this variable, multiple estimates are fit to the borehole data. These estimates gave a reasonable range to include in the analysis, and Fig. 3 shows the area covered by the variogram parameters simulated. This figure shows that the simulated variograms are a close fit to the measured data. All three of the parameters (horizontal range, vertical range, and nugget effect) are simulated independently, and are based on estimates from the recorded borehole data.

Fig. 3 shows the area covered by the variogram parameters, depending on the range and nugget of a given scenario. This range is overlaid on the empirical data for a case of f_s data in the horizontal direction. For this case, the metaparameters used are a lag separation of 1, lag tolerance of 0.5,

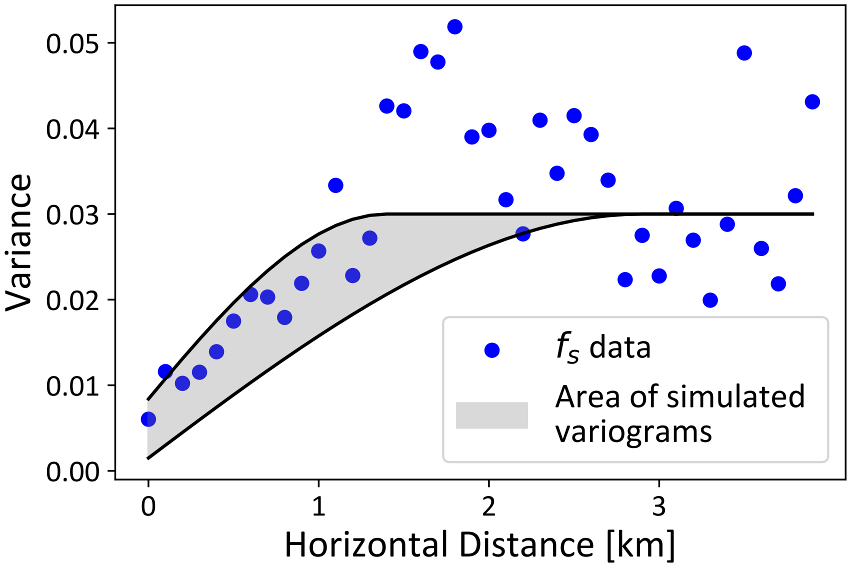

Fig. 3. Range of simulated variograms, based on combination of variogram parameters, overlaid on empirical variogram data from f_s. Empirical data is collected with a lag of 1 and a lag tolerance of 0.5.

and a wide angle to capture all directions in the horizontal plane. For the vertical variogram, the angle is narrower to capture only down each individual borehole. Figures for the combination of parameters and directions are included in Figures S1-S4.

Ground Motions

Earthquake simulations are performed using a python package, pypsha (Sharma 2023), to obtain ground motions from OpenSHA (Field et al. 2003). The source model utilized is the Uniform California Earthquake Rupture Forecast, Version 2 (Field et al. 2003), and a minimum magnitude of 5.0 is used for this application to residential buildings (Green and Bommer 2019). The ground motion models we use are for PGA, from Abrahamson et al. (2014), Boore et al. (2014), and Chiou and Youngs (2014). Each model is equally weighted, and selected based on the generation of a random number for each simulation. We employ the Baker and Jayaram (2008) and Loth and Baker (2013) models for between- and within-event residual spatial correlations, respectively. Since shear wave measurements were taken along the depth of the CPT borings, these measurements were utilized to interpolate $V_{s,30}$ values across the region. First, the largest time measurement of shear wave to surface within 30m of the soil is taken at each point. This measurement at depth z is used to calculate the V_{sz} value, as $z/t(z)$. The V_{sz} value is converted to $V_{s,30}$ using empirical equations in Boore et al. 2011. The $V_{s,30}$ values are then interpolated across the region for application in the ground motion model run.

Groundwater Level

Depth to groundwater is obtained from 18 borehole measurements across Alameda (U.S. Geological Survey 2002). The measurements are dated but without time recorded, so tide is unknown. No information on groundwater fluctuation is provided, so the values are used directly and variance is added in globally, with a uniform shift for each simulation, as documented in Table

1. Based on a California groundwater study, since Alameda is without drainage topographical features, it can be modeled with a flux-controlled groundwater table (Befus et al. 2020), so the height of groundwater is interpolated from a datum. The interpolation is performed using nearest-neighbor interpolation using code from the SimCenter (McKenna et al. 2022). Research in the Bay Area indicates that in urban areas such as Alameda, seasonal groundwater variation is less than 1m, and the 90% confidence of well levels falls 2m above and below the seasonal mean (Greenfield et al. 2023). Thus, for Alameda, we use a uniform variation of 2m above and below the fitted groundwater table to proxy the tidal and seasonal variation and their uncertainty.

Liquefaction Potential

Two LPI models are utilized to account for model uncertainty (Moss et al. 2006; Boulanger and Idriss 2014). For each Monte Carlo simulation, a model is sampled, with equal probability of each. The empirical liquefaction equations (Moss et al. 2006; Boulanger and Idriss 2014) calculate CSR and CRR. The CSR and CRR values are used here to calculate LPI using Eqs. 2 and 3. This process is performed in order to harmonize the outputs of the two models. According to both empirical equations, a soil behavior type index (I_C) cutoff of 2.6 is used to indicate whether the soil falls in a susceptible type (Robertson and Wride 1998; Robertson 2009). Soil layers with an I_C above 2.6 are not liquefiable and are given an FS of one. The Boulanger and Idriss (2014) model uses a soil parameter, C_{FC}, to describe the fines content. This parameter relies on unknown lab data, so it is varied at the widest proposed range from -0.3 to 0.3. This combination of parameter and model uncertainty accounts for the epistemic uncertainty in the liquefaction model.

Hazard and Risk Analysis

For each residential building and each Monte Carlo simulation from the prior steps, a loss ratio is computed that considers possible damage from both ground shaking and liquefaction. The PGA value and LPI value for each building are taken from the grid point closest to the building. Shaking and liquefaction loss ratios are then computed and combined as described below. The loss ratio is the repair cost as a fraction of building value, and is multiplied by the building value to get a dollar loss.

For ground shaking impacts to the buildings, the loss ratio from rupture j ($LR_{gs,j}$) is determined using Hazus fragility functions (FEMA 2020). Building attributes of code level and structural type are assigned based on the known occupancy and year of construction (Alameda County Assessor's Office 2021), and given the distributions of structural type and code level based on Hazus documentation (FEMA 2002).

For liquefaction impacts, a vulnerability function is applied to all buildings to approximate the regional loss and expected annual loss due to liquefaction. The equation for loss ratio, LR, is

$$LR_{liq,j} = 0.117 \times LPI_j^{0.46} \tag{12}$$

where LPI is the LPI value calculated for the point closest to a given building, and loss is calculated by multiplying LR with the building value. The values for this function are approximated from the vulnerability function used in Geyin et al. 2020. Since the vulnerability function reflects total loss, and may include the damage from ground shaking as well as ground failure, to estimate loss ratios from both ground shaking and liquefaction hazards, the total loss ratio is calculated as the maximum of the two above values,

$$LR_j = \max(LR_{gs,j}, LR_{liq,j}) \tag{13}$$

This total loss ratio, LR_j is utilized for the loss analysis and regional outcomes.

Rate of Liquefaction

Fig. 4 shows the rates of liquefaction for the entire study area, as computed using Eq. 5. Generally, the western side of the island and the edges nearest to the coastline have the highest rates, meaning that they are most susceptible to liquefaction.

Fig. 4. Annual rate of liquefaction occurrence, as computed using Eq. 5. The lightest color refers to the lowest rates and therefore lower probability of liquefaction, and darker signifies higher rates or more hazardous areas.

In comparison to past geology-based studies, we see similar spatial results without incorporating the geologic units as hard edges. However, we do see a smoother hazard and higher hazard in the dune sand in the middle of Alameda. When looking at only the M7.1 events modeled, which contain variability in other parameters, points within the artificial fill exceed an LPI of 15, on average, 19% of the time. In comparison, the dune sand exceeds an LPI of 15, on average, 7% of the time. The average LPI in the artificial fill for a M7.1 event is 7.3 compared to 3.7 in the dune sand, which falls lower than the liquefaction threshold. While differences are less stark than in geology-based studies (e.g. Holzer et al. 2006), this method incorporates more modeling uncertainty, includes probabilistic ground shaking hazard, and considers spatial variation that is not included in models based solely on samples.

Regional Severity

The regional-scale metric is shown in Fig. 5, with the annual rate of a given portion of land area, on the x-axis, exceeding a certain LPI threshold, on the y-axis. This rate is constructed for the entire region of interest using Eq. 7. LPI thresholds of 5 and 15 are typically used to signify moderate and high liquefaction severity, respectively. Thus, an area with LPI above 5 is likely to have moderate liquefaction, and an area with LPI above 15 is likely to have severe liquefaction. We see that it is unlikely that over 80% of the land area exceeds an LPI of 5. However, there is about a 0.06 annual rate of more than 30% of the land area exceeding that same threshold. This metric can be used to compare along either direction, such as holding the LPI threshold constant and determining the probability of various land areas exceeding that threshold.

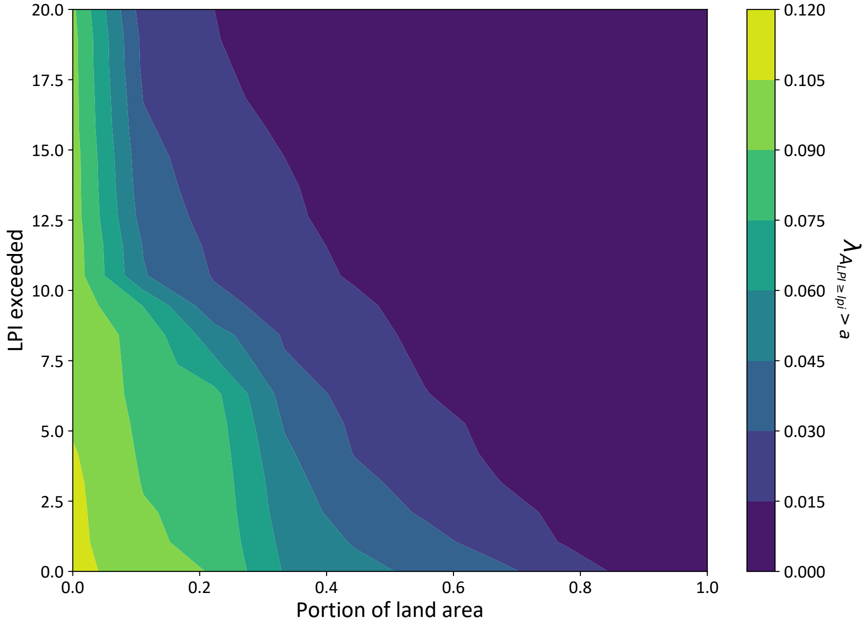

Fig. 5. Exceedance rate of combinations of portions of land area within the island exceeding LPI thresholds, as computed using Eq. 7. LPI thresholds of 5 and 15 can be interpreted as moderate and severe liquefaction, respectively.

This regional severity metric combines the site-specificity of LPI calculations with regional information that can be used on a large scale to understand the probability of liquefaction effects. This metric is also useful to understand the space and the variety of potential situations that may occur. It is equally likely that 50% of the island experiences $LPI > 5$ as it is that 20% of the island experiences $LPI > 15$. There is a large range of possible ruptures, and this metric allows a visual and probabilistic representation of the distribution of their outcomes with regard to severity and extent.

Disaggregation of Earthquakes Triggering Liquefaction

We disaggregate the simulations with a specified area exceeding an LPI threshold. Fig. 6 shows the contributions of earthquakes from various magnitudes and distances to four levels of regional impact. Fig. 6a and Fig. 6c show 30% of the study area exceeding an LPI of 5 and 10% of the area exceeding LPI of 15, respectively. These two hazards have approximately the same annual rate of occurrence, 0.06. Fig. 6b and Fig. 6d show 60% of the area exceeding an LPI of 5 and 35% of the area exceeding LPI of 15, respectively. These two hazards correspond to an annual rate of approximately 0.015. Note that the axes for Figs 6a and 6c include larger rupture distances, as more distant sources contribute to exceedances of the higher rate impacts. For the Alameda case, distances between 5-10km are associated with Hayward fault ruptures and distances of 20-25km usually map to the San Andreas fault. In comparing Figs 6a and 6b, ruptures with a wider range of characteristics contribute to the lower LPI threshold, but the largest contributors for the higher LPI threshold are coming from rupture distances between 0 and 10km, or the Hayward fault. Generally, as LPI and area thresholds increase, the disaggregation trends towards closer faults and larger magnitude ruptures.

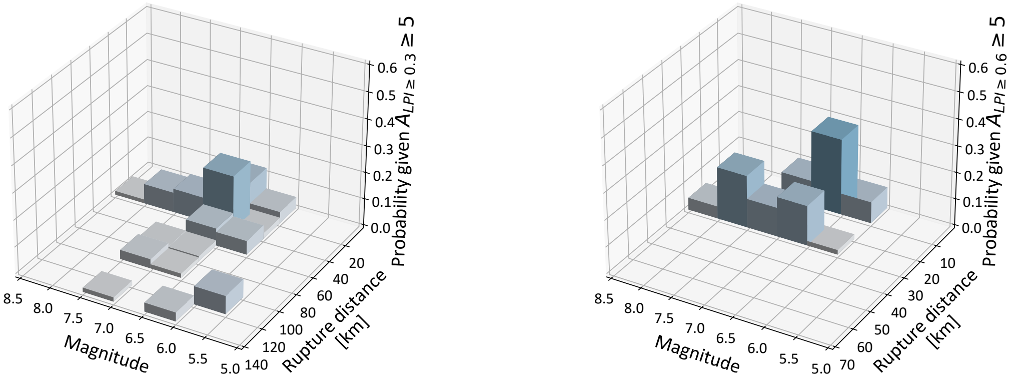

(a) 30% area exceeding LPI of 5.

(b) 60% area exceeding LPI of 5.

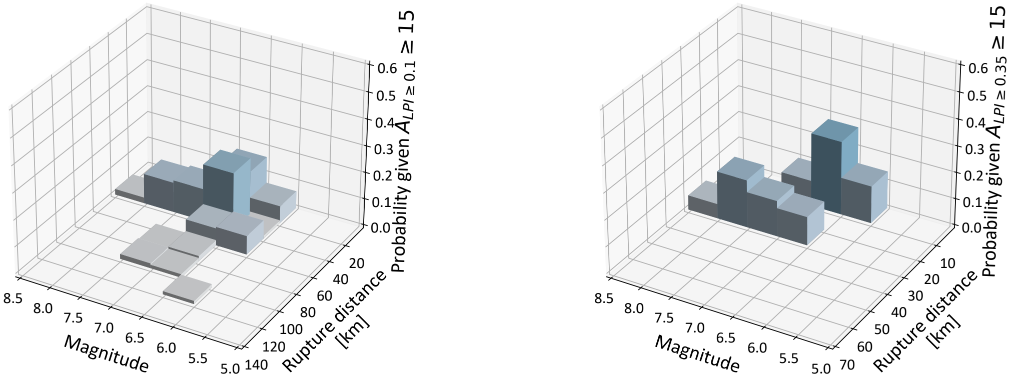

(c) 10% area exceeding LPI of 15.

(d) 35% area exceeding LPI of 15.

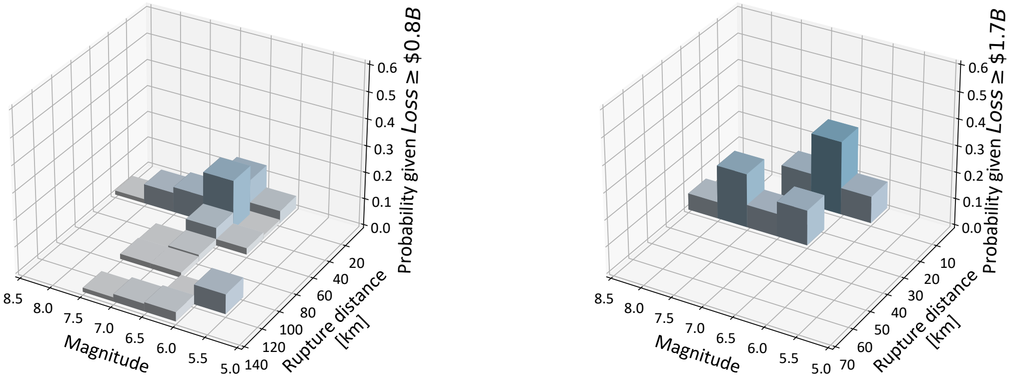

(e) Total loss exceeding 0.8 Billion USD.

(f) Total loss exceeding 1.7 Billion USD.

Fig. 6. Disaggregation plots for the magnitude and source-site distance of triggering earthquakes. Only bins contributing more than 0.01 are plotted. Note that the rupture distance range is larger for plots 6a,c,and e.

Fig. 6 shows that contributions to these liquefaction outcomes can come from very large (and rare) ruptures as well as (more frequent) distant and lower-magnitude ruptures. In scenario studies that do not consider probabilistic ruptures, the range of possibilities is not typically considered, and the vulnerability of some areas may be underestimated. Additionally, it is important to consider not only the largest contribution to the ground shaking hazard (as in traditional seismic hazard disaggregation), but also to the ground failure.

Disaggregation can also be performed on community-level loss. Figs. 6e and 6f show the seismic sources causing losses exceeding 0.8 Billion USD and 1.7 Billion USD. The annual rates of these losses correspond with the annual rates of 30% area over LPI of 5 or 10% area over LPI of 15 and 60% of area over LPI of 5 or 35% of area over LPI of 15, respectively (Figs. 6a,c,e and Figs. 6b,d,f.). A similar trend appears as with the hazard disaggregation, so the regional-scale metric, rate of portion of land area exceeding LPI threshold, may be used as a proxy in cases without sufficient data to perform full loss analysis.

A common practice in planning is to use scenarios to represent hazard in place of a full probabilistic analysis (e.g. U.S. Geological Survey 2022; Federal Emergency Management Agency (FEMA) 2010; Federal Emergency Management Agency (FEMA) 2020). The above disaggregation calculations can inform what sources contribute the most to the regional hazard of interest. Thus, the hazard appears to come mostly from the nearby Hayward fault, which has been used in scenario planning for this area (e.g. Hudnut et al. 2018). However, considering this source alone misses some of the hazardous simulations, namely those with a large spread of LPI exceeding 15 (Figs. 6c and 6d) and therefore does not consider those distributions of impact. This disaggregation can be used to inform scenarios that may prioritize a farther source based on the extent and severity of interest.

Loss Analysis

The computed loss ratios for each rupture are used in Eq. 9 to compute expected annual loss ratios. Fig. 7 shows the expected annual loss ratio, $E[LR]$ of residential buildings from both ground shaking damage and liquefaction. These losses consider the hazard as well as the exposure, accounting for the building locations, structural types, and years of construction.

While Fig. 4 shows that the western side of Alameda has high liquefaction hazard, it does not contribute to losses here because it does not have residential buildings. The risk is higher in many of the locations with lower return periods of liquefaction, but there is additional variation that comes from the building exposure as well as the ground shaking hazard.

Fig. 8 shows the portion of expected loss that is attributable to liquefaction hazard, $E[LR_{liq}]/E[LR]$, where $E[LR_{liq}]$ is calculated as in Eqn. 10 and $E[LR]$ is calculated as in Eqn. 9. This portion of expected loss generally follows the pattern of the liquefaction hazard, though some cases such as newer buildings have greater liquefaction than ground shaking vulnerability. This building-level analysis can support identification of protective measures for the community.

In addition to building-level loss analysis, the total community loss can be calculated for each simulation (Eq. 11). Fig. 9 shows the exceedance rates of total community loss values. The black curve represents the total loss that a community may face given the exceedance rates of each rupture. The annual rate of liquefaction is 0.111. Most (96%) ruptures result in some loss, and almost 70% of the ruptures result in loss of over 10% of the total residential building value.

The curves for $Loss_{gs}$ and $Loss_{liq}$ are determined using LR_{gs} and LR_{liq}, respectively. For losses less than 0.7 billion dollars, the liquefaction and total loss curves are very similar. However,

Fig. 7. Map of expected annual loss ratio at each residential building location. The darker color corresponds to the higher $E[LR]$ values, and lighter colors signify a lower expected loss. Non-colored locations are areas without residential buildings.

for losses greater than 1 billion dollars, the total loss rates exceed and outpace the rates from ground shaking or liquefaction loss alone. This finding emphasizes the need to consider both ground shaking and liquefaction as part of earthquake loss analysis.

Sensitivity Analysis

Input parameter values are varied through the analyses to determine the most important sources of uncertainty on the output liquefaction maps. Table 1 shows the uncertain parameters in each of these input categories for the case study, as well as the type and range of variance included. Uncertainty is included within interpolation processes and within variable assignment. Only parameters of epistemic uncertainty, which can be controlled by modeling choices, are included. Aleatory variability, such as the characteristics of the triggering earthquake, is not included here.

The distance-based general sensitivity analysis (DGSA) provides insight into which input parameters are the most important to the output. The most important inputs are those that have the largest impact on the output maps, measured as the difference between the normalized area between CDFs of inputs for output clusters. Fig. 10 shows the sensitivity values of each of the seven uncertain input variables for three clusters. The sensitivity analysis is performed using bootstrapping to generate confidence intervals and stable output. Ninety percent confidence intervals are reported as the black lines on each bar. Those with the highest values, empirical liquefaction model and ground motion model, are the most influential in determining the output LPI map.

From Fig. 10, the most influential variable, and only variable that is important with 90%

Fig. 8. Map of the expected fraction of building loss ratio attributable to liquefaction hazard.

TABLE 1. Uncertain parameters included in liquefaction workflow.

Category	Variable	Uncertain range/ Modeling source
Ground motions	Ground motion model	Abrahamson et al. (2014), Boore et al. (2014), or Chiou and Youngs (2014)
Groundwater	Water table shift [m]	U[-2,2]
Soil	Variogram horizontal range [km]	U[1.5,3.0]
	Variogram vertical range [m]	U[10,20]
	Variogram nugget	U[0.0001,0.2]
Liquefaction	Empirical equation	Moss et al. (2006) or Boulanger and Idriss (2014)
	Fines content constant (C_{FC})	U[-0.3,0.3]

confidence, is the empirical equation used to calculate LPI. Thus, a strong predictor of a regional map having high or low liquefaction potential is the equation used to calculate LPI. The liquefaction equation that is used is an important choice, and employing a single equation obscures some uncertainty in liquefaction modeling. Future regional risk studies should consider utilizing multiple empirical liquefaction equations to account for this modeling uncertainty.

The second variable impacting the output liquefaction map is the ground motion model that is used for the simulation. It is interesting that the two model choices are the most important, above the more physical or site-specific modeling choices. As is best practice in earthquake engineering, it is important that regional liquefaction studies utilize multiple ground motion models to reduce

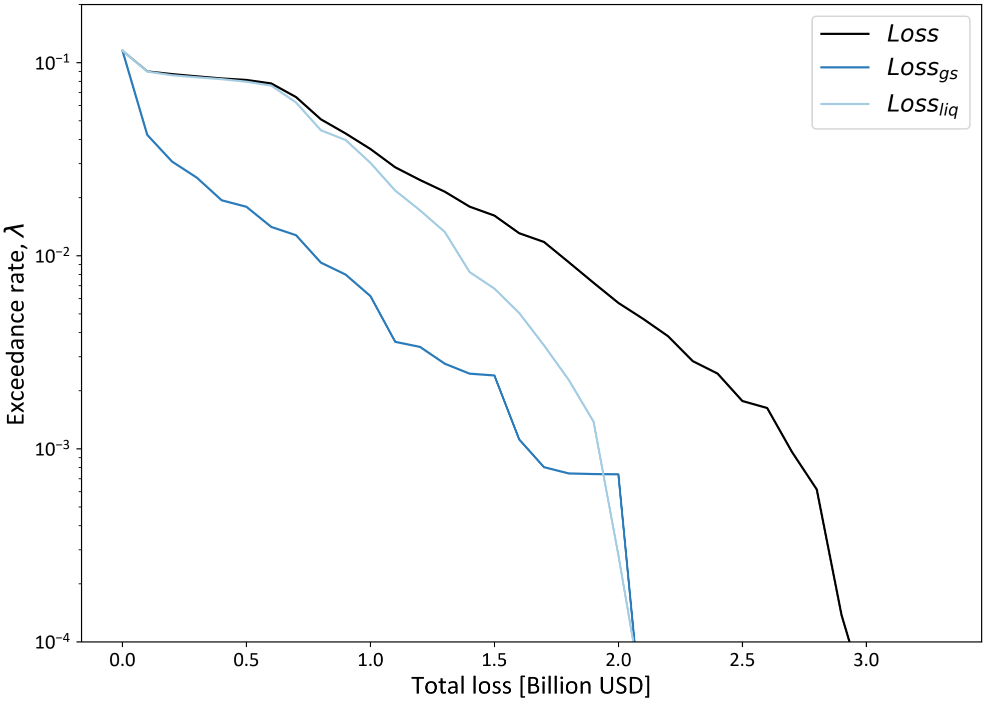

Fig. 9. Loss exceedance curves for total community losses due to earthquake ground shaking alone, liquefaction alone, and combined.

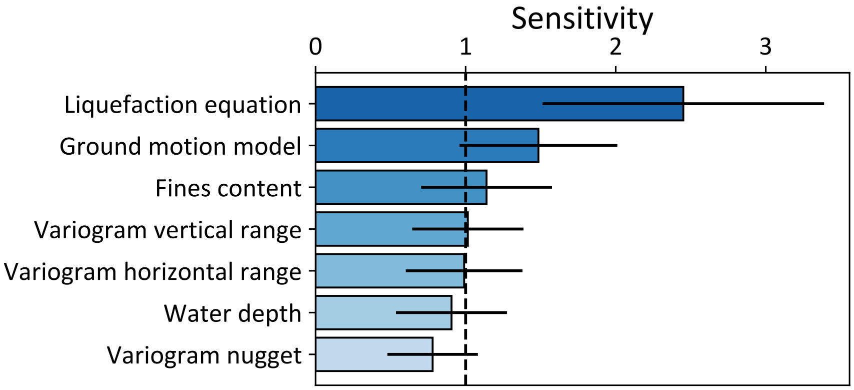

Fig. 10. Sensitivity values for each input variable from DGSA with three clusters. The output is most sensitive to the variables with the highest values. The output values used are the principal components explaining 99% of the variance in the regional output maps. The black lines on each bar represent the 90% confidence intervals on the sensitivity estimates.

bias in regional results.

CONCLUSIONS

In this paper, we demonstrate the application of liquefaction potential index (LPI) calculations to assess risk on a regional scale while considering modeling uncertainty. This analysis utilizes

Monte Carlo simulations to include variability in unknown ground shaking, groundwater, and soil parameters. A probabilistic set of ruptures and multiple ground motion models provide simulated ground motions. Groundwater is interpolated from measured data across the study area. Soil models are generated on a 3D grid for use in calculations of LPI across the case study area. Epistemic uncertainty from modeling parameters is carried through to determine the sensitivity of output LPI maps to those parameters. Through the regional analysis, we calculate occurrence rates for a proposed metric that captures the extent and severity of liquefaction. The hazard model is integrated with both ground shaking and liquefaction fragility and loss functions to determine damage and loss to residential buildings, providing the ability to separate losses from ground shaking and liquefaction and to determine expected annual loss at a per-building and a regional level.

This study shows how a regional liquefaction analysis can be performed from limited input borehole data. We introduce a regional metric accounting for LPI thresholds exceeded by different areas of the region; this metric enables us to compute exceedance rates for varying extents and severity of hazard. We propagate the hazard extent to expected losses of residential buildings to quantify building-level and regional risk.

We apply the model to a case study in Alameda, CA to demonstrate how liquefaction contributes to total earthquake risk. We find from disaggregation calculations that risk for Alameda comes primarily from earthquakes on the Hayward and San Andreas faults, from both commonly considered ruptures and others. Additionally, the disaggregation of seismic source shows that the triggering earthquakes for various extents of liquefaction come from many distant ruptures in addition to the high magnitude, nearby ruptures. Thus, future studies should employ probabilistic analysis to capture the sources and distributions of liquefaction from numerous earthquake ruptures.

Based on the sensitivity analysis, regional results are sensitive to the liquefaction equation that is used to determine LPI and the ground motion model used to generate peak ground accelerations. Therefore, multiple equations should be considered to capture epistemic uncertainties in regional risk results. These sensitivity results point to important inputs that should be considered in future studies, especially the variance in liquefaction and ground motion models. A similar sensitivity analysis should be performed in different locations to determine the generalizability of these results.

DATA AVAILABILITY STATEMENT

Some or all data, models, or code generated or used during the study are available in a repository online in accordance with funder data retention policies (Mongold 2023).

ACKNOWLEDGEMENTS

The authors thank Laurie Baise, Kevin Befus, Scott Brandenberg, Brett Maurer, Anne Wein, and Liam Wotherspoon for feedback, data, and helpful discussions. The authors thank Neetesh Sharma for help with the ground motion generation and Ádám Zsarnóczay for help with nearest neighbor interpolation. This material is based upon work supported by the National Science Foundation under Grants No. DGE-1656518 and CMMI-2053014. Any opinions, findings, and conclusions or recommendations expressed in this material are those of the authors and do not necessarily reflect the views of the National Science Foundation.

SUPPLEMENTAL MATERIALS

A detailed explanation of variogram fitting and Figs. S1-S4 are available online in the ASCE Library (`ascelibrary.org`).

REFERENCES

Abrahamson, N., Silva, W., and Kamai, R. (2014). “Summary of the ask14 ground motion relation for active crustal regions.” *Earthquake Spectra*, 30(3), 1025–1055.

Alameda County Assessor’s Office (2021). “Alameda county parcel viewer, <https://www.acassessor.org/homeowners/assessment-resources/parcel-viewer/>.

Andrus, R. D., Mohanan, N. P., Piratheepan, P., Ellis, B. S., and Holzer, T. L. (2007). “Predicting shear-wave velocity from cone penetration resistance.” *Proceedings of the 4th international conference on earthquake geotechnical engineering, Thessaloniki, Greece*, Vol. 2528.

Baise, L., Higgins, R., and Brankman, C. (2006). “Liquefaction hazard mapping—statistical and spatial characterization of susceptible units.” *Journal of Geotechnical and Geoenvironmental Engineering*, 132(6), 705–715.

Baker, J. and Faber, M. (2008). “Liquefaction risk assessment using geostatistics to account for soil spatial variability.” *Journal of Geotechnical and Geoenvironmental Engineering*, 134(1), 14–23.

Baker, J. and Jayaram, N. (2008). “Correlation of spectral acceleration values from nga ground motion models.” *Earthquake Spectra*, 24(1), 299–317.

Baker, J. W., Bradley, B., and P.J., S. (2021). *Seismic Hazard and Risk Analysis*. Cambridge University Press, New York, NY.

Befus, K. M., Barnard, P. L., Hoover, D. J., Finzi Hart, J. A., and Voss, C. I. (2020). “Increasing threat of coastal groundwater hazards from sea-level rise in California.” *Nature Climate Change*, 10(10), 946–952.

Beyzaei, C., Bray, J., Cubrinovski, M., Bastin, S., Stringer, M., Jacka, M., van Ballegooy, S., Riemer, M., and Wentz, R. (2020). “Characterization of silty soil thin layering and groundwater conditions for liquefaction assessment.” *Canadian Geotechnical Journal*, 57(2), 263–276.

Bird, J., Bommer, J., Crowley, H., and Pinho, R. (2006). “Modelling liquefaction-induced building damage in earthquake loss estimation.” *Soil Dynamics and Earthquake Engineering*, 26(1), 15–30.

Boore, D., Stewart, J., Seyhan, E., and Atkinson, G. (2014). “Nga-west2 equations for predicting pga, pgv, and 5% damped psa for shallow crustal earthquakes.” *Earthquake Spectra*, 30(3), 1057–1085.

Boore, D. M., Thompson, E. M., and Cadet, H. (2011). “Regional correlations of vs 30 and velocities averaged over depths less than and greater than 30 meters.” *Bulletin of the Seismological Society of America*, 101(6), 3046–3059.

Boulanger, R. and Idriss, I. (2014). “Liquefaction susceptibility criteria for silts and clays.” *Journal of Geotechnical and Geoenvironmental Engineering*, 132(11), 1413–1426.

Bozzoni, F., Bonì, R., Conca, D., Meisina, C., Lai, C. G., and Zuccolo, E. (2021). “A geospatial approach for mapping the earthquake-induced liquefaction risk at the european scale.” *Geosciences*, 11(1), 32.

Bullock, Z., Zimmaro, P., Lavrentiadis, G., Wang, P., Ojomo, O., Asimaki, D., Rathje, E., and Stewart, J. (2023). “A latent gaussian process model for the spatial distribution of liquefaction manifestation.” *Earthquake Spectra*, 39(2), 1189–1213.

Chiou, B. S.-J. and Youngs, R. R. (2014). “Update of the chiou and youngs nga model for the average horizontal component of peak ground motion and response spectra.” *Earthquake Spectra*, 30(3), 1117–1153.

Chung, J.-W. and Rogers, J. (2013). “Influence of assumed groundwater depth on mapping liquefaction potential." *Environmental & Engineering Geoscience*, 19(4), 377–389.

Cubrinovski, M., Bray, J., De La Torre, C., Olsen, M., Bradley, B., Chiaro, G., Stocks, E., and Wotherspoon, L. (2017). "Liquefaction effects and associated damages observed at the Wellington CentrePort from the 2016 Kaikoura earthquake." *Bulletin of the New Zealand Society for Earthquake Engineering*, 50(2), 152–173.

Cubrinovski, M., Bray, J., Taylor, M., Giorgini, S., Bradley, B., Wotherspoon, L., and Zupan, J. (2011). "Soil liquefaction effects in the central business district during the February 2011 Christchurch earthquake." *Seismological Research Letters*, 82(6), 893–904.

Cubrinovski, M., Henderson, D., and Bradley, B. (2012). "Liquefaction impacts in residential areas in the 2010-2011 Christchurch earthquakes.

Federal Emergency Management Agency (FEMA) (2010). "Developing and Maintaining Emergency Operations Plans. [Online; accessed 9-May-2023].

Federal Emergency Management Agency (FEMA) (2020). "Guidance for Flood Risk Analysis and Mapping. [Online; accessed 9-May-2023].

FEMA (2002). *Hazus-MH 2.1 Technical Manual*. Department of Homeland Security, Federal Emergency Management Agency, Washington, D.C.

FEMA (2020). *Hazus Earthquake Model Technical Manual*. Federal Emergency Management Agency.

Fenwick, D., Scheidt, C., and Caers, J. (2014). "Quantifying asymmetric parameter interactions in sensitivity analysis: Application to reservoir modeling." *Mathematical Geosciences*, 46(4), 493–511.

Field, E., Jordan, T., and Cornell, C. (2003). "OpenSHA: A developing community-modeling environment for seismic hazard analysis." *Seismological Research Letters*, 74(4), 406–419.

Geyin, M. and Maurer, B. (2020). "Fragility functions for liquefaction-induced ground failure." *Journal of Geotechnical and Geoenvironmental Engineering*, 146(12), 04020142.

Geyin, M., Maurer, B., and van Ballegooy, S. (2020). "Lifecycle liquefaction hazard assessment and mitigation." *Geo-Congress 2020*, Reston, VA:American Society of Civil Engineers, 312–320.

Goda, K., Atkinson, G. M., Hunter, J., Crow, H., and Motazedian, D. (2011). "Probabilistic liquefaction hazard analysis for four Canadian cities." *Bulletin of the Seismological Society of America*, 101(1), 190–201.

Grant, A., Wein, A., Befus, K., Hart, J., Frame, M., Volentine, R., Barnard, P., and Knudsen, K. (2021). "Changes in liquefaction severity in the San Francisco Bay area with sea-level rise." *Geo-Extreme 2021*, Savannah, Georgia, American Society of Civil Engineers, 308—317.

Green, R. and Bommer, J. (2019). "What is the smallest earthquake magnitude that needs to be considered in assessing liquefaction hazard?." *Earthquake Spectra*, 35(3), 1441—1464.

Greenfield, M. and Grant, A. (2022). "Regional-scale liquefaction analyses." *Geo-Congress 2022*, Charlotte, North Carolina, American Society of Civil Engineers, 401—410.

Greenfield, M. W., Estep, T., Hitchcock, C. S., Wilson, J. M., Leshchinsky, B., Wartman, J., Wade, A., Kottke, A., and Boone, M. (2023). "Spatiotemporal groundwater modeling for hazard analyses in the San Francisco Bay region." *Authorea Preprints*.

Holzer, T., Noce, T., and Bennett, M. (2011). "Liquefaction probability curves for surficial geologic deposits." *Environmental and Engineering Geoscience*, 17(1), 1–21.

Holzer, T., Toprak, S., and Bennett, M. (2002). "Liquefaction potential index and seismic hazard mapping in the San Franciscco Bay area, California." *7th National Conference on Earthquake Engineering*, 1699–1706 (Jul).

Holzer, T. L., Bennett, M. J., Noce, T. E., Padovani, A. C., and Tinsley III, J. C. (2006). "Liquefaction hazard mapping with LPI in the greater Oakland, California, area." *Earthquake Spectra*, 22(3), 693–708.

Hudnut, K., Wein, A., Cox, D., Porter, K., Johnson, L., Perry, S., Bruce, J., and LaPointe, D. (2018). "The haywired earthquake scenario—we can outsmart disaster." *Report No. 2018-3016*, US Geological Survey.

Iwasaki, T., Tatsuoka, F., Tokida, K., and Yasuda, S. (1978). "A practical method for assessing soil liquefaction potential." *Proceedings of the second International Conference on Microzonation for Safer Construction, Research, and Application*, 885–896.

Kim, H.-S., Kim, M., Baise, L., and Kim, B. (2021). "Local and regional evaluation of liquefaction potential index and liquefaction severity number for liquefaction-induced sand boils in pohang, south korea." *Soil Dynamics and Earthquake Engineering*, 141, 106459.

Knudsen, K. L., Sowers, J. M., Witter, R. C., Wentworth, C. M., Helley, E. J., Wentworth, C. M., Nicholson, R. S., Wright, H. M., and Brown, K. H. (2000). "Preliminary maps of quaternary deposits and liquefaction susceptibility, nine-county San Francisco Bay region, California: A digital database." *Open-File Report 00-444*, U.S. Geological Survey.

Koutsourelakis, S., Prévost, J. H., and Deodatis, G. (2002). "Risk assessment of an interacting soil-structure system due to liquefaction." *Earthquake Engng Struct. Dyn.*, 31, 851–879.

Kramer, S. and Mayfield, R. (2007). "Return period of soil liquefaction." *Journal of Geotechnical and Geoenvironmental Engineering*, 133(7), 802—813.

Lenz, J. and Baise, L. (2007). "Spatial variability of liquefaction potential in regional mapping using CPT and SPT data." *Soil Dynamics and Earthquake Engineering*, 27(7), 690–702.

Li, D., Juang, C., and Andrus, R. (2006). "Liquefaction potential index : A critical assessment using probability concept." *Journal of GeoEngineering*, 1(1), 11–24.

Loth, C. and Baker, J. W. (2013). "A spatial cross-correlation model of spectral accelerations at multiple periods." *Earthquake Engineering & Structural Dynamics*, 42(3), 397–417.

Makdisi, A. (2021). "Liquefaction-targeted ground motion parameters." Ph.d. thesis, University of Washington, Washington (July).

Maurer, B., Green, R., Cubrinovski, M., and Bradley, B. (2014). "Evaluation of the liquefaction potential index for assessing liquefaction hazard in Christchurch, New Zealand." *Journal of Geotechnical and Geoenvironmental Engineering*, 140(7), 04014032.

McKenna, F., Zsarnóczay, A., Zhong, K., Gardner, M., Yi, S., Satish, A. B., Gavrilovic, S., and Elhaddad, W. (2022). "NHERI-SimCenter/BackendApplications: Version 4.0.0, <https://github.com/NHERI-SimCenter/BackendApplications/releases/tag/v4.0.0>.

Mongold, E. (2023). "regional_liquefaction v1.0.0, <https://zenodo.org/records/8411309>.

Moss, R., Seed, R., Kayen, R., Stewart, J., Der Kiureghian, A., and Cetin, K. (2006). "CPT-based probabilistic and deterministic assessment of in situ seismic soil liquefaction potential." *J. Geotech. Goenviron. Eng.*, 132(8), 1032–1051.

Mussa, K. R., Mjemah, I. C., and Muzuka, A. N. N. (2020). "A review on the state of knowledge, conceptual and theoretical contentions of major theories and principles governing groundwater flow modeling." *Applied Water Science*, 10(6), 1–10.

National Academies of Sciences, Engineering, and Medicine (2021). *State of the Art and Practice in the Assessment of Earthquake-Induced Soil Liquefaction and Its Consequences*. National Academies Press, Washington, D.C.

Phoon, K.-K. and Kulhawy, F. (1999). "Characterization of geotechnical variability." *Canadian*

Geotechnical Journal, 36(4), 612–624.

Robertson, P. (2009). “Performance based earthquake design using the CPT.” *Proc. IS-Tokyo*, 3–20.

Robertson, P. and Campanella, R. (1985). “Liquefaction potential of sands using the CPT.” *J. Geotech. Engrg.*, 111(3), 384–403.

Robertson, P. K. and Wride, C. (1998). “Evaluating cyclic liquefaction potential using the cone penetration test.” *Canadian geotechnical journal*, 35(3), 442–459.

Sahir, H. and Pak, A. (2010). “Estimating liquefaction-induced settlement of shallow foundations by numerical approach.” *Computers and Geotechnics*, 37, 267–279.

Setiawan, H., Serikawa, Y., Nakamura, M., Miyajima, M., and Yoshida, M. (2017). “Structural damage to houses and buildings induced by liquefaction in the 2016 Kumamoto Earthquake, Japan.” *Geoenvironmental Disasters*, 4, 1–12.

Sharma, N. (2023). “pypsha, <https://github.com/neetesh-nks/pypsha>.

Todorovic, L. and Silva, V. (2022). “A liquefaction occurrence model for regional analysis.” *Soil Dynamics and Earthquake Engineering*, 161, 107430.

Toprak, S. and Holzer, T. (2003). “Liquefaction potential index: Field assessment.” *J. Geotech. Geoenviron. Eng.*, 129(4), 315–322.

U.S. Geological Survey (2002). “Table of CPT data: Alameda county, <https://earthquake.usgs.gov/research/cpt/data/alameda/table/>.

U.S. Geological Survey (2022). “Earthquake Scenarios. [Online; accessed 9-May-2023].

van Ballegooy, S., Wentz, F., and Boulanger, R. W. (2015). “Evaluation of CPT-based liquefaction procedures at regional scale.” *Soil Dynamics and Earthquake Engineering*, 79, 315—334.

Wang, C. and Chen, Q. (2018). “A hybrid geotechnical and geological data-based framework for multiscale regional liquefaction hazard mapping.” *Géotechnique*, 68(7), 614–625.

Wang, C., Chen, Q., Shen, M., and Juang, C. (2017). “On the spatial variability of CPT-based geotechnical parameters for regional liquefaction evaluation.” *Soil Dynamics and Earthquake Engineering*, 95, 153–166.

Witter, R., Knudsen, K., Sowers, J., Wentworth, C., Koehler, R., and C.E., R. (2006). “Maps of quaternary deposits and liquefaction susceptibility in the central San Francisco Bay region, California.” *Report No. 2006-1037*, U.S. Geological Survey.

Yilmaz, C., Silva, V., and Weatherill, G. (2021). “Probabilistic framework for regional loss assessment due to earthquake-induced liquefaction including epistemic uncertainty.” *Soil Dynamics and Earthquake Engineering*, 141.

Zhu, J., Baise, L., and Thompson, E. (2017). “An updated geospatial liquefaction model for global application.” *Bulletin of the Seismological Society of America*, 107(3), 1365–1385.

Zhu, J., Daley, D., Baise, L., Thompson, E., Wald, D., and Knudsen, K. (2015). “A geospatial liquefaction model for rapid response and loss estimation.” *Earthquake Spectra*, 31(3), 1813––1837.